

PAPER

Effects of composition and temperature on the exciton emission behaviors of $\text{Mo}(\text{S}_x\text{Se}_{1-x})_2$ monolayer: experiment and theory

To cite this article: Fangfang Chen *et al* 2020 *Nanotechnology* **31** 155703

View the [article online](#) for updates and enhancements.



IOP | ebooks™

Bringing you innovative digital publishing with leading voices to create your essential collection of books in STEM research.

Start exploring the collection - download the first chapter of every title for free.

Effects of composition and temperature on the exciton emission behaviors of $\text{Mo}(\text{S}_x\text{Se}_{1-x})_2$ monolayer: experiment and theory

Fangfang Chen¹, Bin Zhou¹, Peng Zhang², Yan Ye¹, Huimin Sun¹,
Liping Xu¹, Liangqing Zhu¹, Kai Jiang^{1,5}, Yongji Gong²,
Zhigao Hu^{1,3,4,5}  and Junhao Chu^{1,3,4}

¹ Technical Center for Multifunctional Magneto-Optical Spectroscopy (Shanghai), Department of Materials, School of Physics and Electronic Science, East China Normal University, Shanghai 200241, People's Republic of China

² School of Materials Science & Engineering, Beihang University, Beijing 100191, People's Republic of China

³ Collaborative Innovation Center of Extreme Optics, Shanxi University, Taiyuan, Shanxi 030006, People's Republic of China

⁴ Shanghai Institute of Intelligent Electronics & Systems, Fudan University, Shanghai 200433, People's Republic of China

E-mail: kjiang@ee.ecnu.edu.cn and zghu@ee.ecnu.edu.cn

Received 1 August 2019, revised 4 November 2019

Accepted for publication 20 December 2019

Published 22 January 2020



CrossMark

Abstract

Exploring the excitonic behavior of two-dimensional (2D) alloys is of great significance, which not only could promote the understanding of fundamental photophysics in optoelectronic devices, but could also guide the functional improvement of future applications. Here, we demonstrate the controllable synthesis of monolayer $\text{Mo}(\text{S}_x\text{Se}_{1-x})_2$ nanosheets using a one-step chemical vapor deposition method and systematical investigation on the exciton emission characteristics based on the temperature-dependent photoluminescence spectroscopy (PL) experiments. As a result, the tunable bandgap of $\text{Mo}(\text{S}_x\text{Se}_{1-x})_2$ alloys between 1.52 and 1.85 eV can be achieved, which is consistent with the theoretical results calculated by the *ab initio* density function theory. Besides, both the exciton and trion behaviors in $\text{Mo}(\text{S}_x\text{Se}_{1-x})_2$ are observed from the PL spectra at $T = 80$ K. More intriguingly, the differences between the emission energy of exciton and trion (ΔE), known as the dissociation energy of the trion, are positively correlated to the concentrations of the sulfur (S) elements, which is also proved by the theoretical calculation. Combining the experimental and theoretical results, the phenomena can be explained by the reduced dielectric screening effect and the increasing Fermi energy (E_F) along with the increasing of sulfur in $\text{Mo}(\text{S}_x\text{Se}_{1-x})_2$ nanosheets, jointly leading to the increase of ΔE . Furthermore, the evolutions of ΔE in $\text{Mo}(\text{S}_x\text{Se}_{1-x})_2$ alloys as a function of temperature have been also discovered, which lay the foundation for the potential uses of 2D alloys in optoelectronic devices.

Supplementary material for this article is available [online](#)

Keywords: exciton emission, two-dimensional alloys, $\text{Mo}(\text{S}_x\text{Se}_{1-x})_2$, temperature dependence

(Some figures may appear in colour only in the online journal)

⁵ Authors to whom any correspondence should be addressed.

1. Introduction

Two-dimensional (2D) materials, characterized by the atomic thickness relying on the weak Van der Waals (VdW) interactions, excellent physical and optoelectronic properties, have triggered much attention nowadays due to the promising use in transistors, photodetectors, electroluminescent devices, and spintronic devices. [1–4] 2D family includes various members, including semi-metallic graphene, semiconductive transition metal dichalcogenides (TMDs), insulative boron nitride (BN), and so on, which creates valuable opportunities for designing desirable configurations and performance, such as 2D heterostructures and 2D alloys. In particular, the fabrication of 2D alloys based on TMDs is believed to realize a wider controllable bandgap than the individual materials, which is beneficial for the development of functional optoelectronics. Recently, Gong *et al* demonstrated that the optical gap change from 1.85 to 1.54 eV is observed in MoS₂ as a function of Selenium (Se) doping. [5] Duan *et al* reported that the band gap of the W(S_xSe_{1-x})₂ alloys can be fully tuned from the pure WSe₂ (1.65 eV) to pure WS₂ (1.98 eV) by the S/Se ratio. [6] However, the in-depth investigation of the physical phenomenon, such as the exciton behaviors in 2D alloys has been rarely performed, which still remains challenges for their fundamental physical applications.

As we know, the synergistic effect among quantum confinement, reduced dielectric screening, as well as the heavy effective masses of carriers result in considerable impact in monolayer TMDs. The high surface-volume ratio in monolayer TMDs exhibits a strong light–matter interaction for exploring the basic physical properties of excess carriers by the nondestructive spectrum technologies. Besides, the excitonic and trionic resonances in monolayer TMDs can be well isolated at room temperature. [7, 8] Therefore, it is believed that monolayer TMDs offer a suitable platform for the investigation of the interaction between exciton and trion, which is of great importance to the design of 2D-based optoelectronics and underlying applications in valleytronics. For example, the impact of the free carrier reservoir on the optical properties of excitonic and trionic complexes in a MoSe₂ monolayer under a cryogenic condition have been studied by modulating electron density by photo-doping method with a non-resonant pump laser. [9] As for 2D alloys, Sun *et al* reported the contrasting behavior in the temperature evolution of excitons and trions PL intensity in sulfur-rich and selenium-rich W(S_xSe_{1-x})₂ alloys. [10] However, the differences between the emission energy of exciton and trion (ΔE), known as the dissociation energy of the trion, as a function of the composition and temperature in ternary TMDCs semiconductor have been rarely reported to date. The exciton emission behaviors in different energy and temperature regions will impact the investigation of phenomena such as exciton condensation and the Fermi-edge singularity. The ability to uncover this character will contribute to the development of a new generation of optoelectronic devices such as light-emitting diodes and excitonic circuits.

In this work, we systematically investigated the exciton emission characteristics of one-step chemical vapor deposition

(CVD)-synthesized 2D Mo(S_xSe_{1-x})₂ monolayer alloys by the PL spectrum technologies and theoretical calculations. The obtained bandgap of Mo(S_xSe_{1-x})₂ monolayer increased from 1.52 to 1.85 eV with the increasing of S concentrations, matches well with the theoretical results. It is emphasized that the evident exciton and trion behaviors can be probed by the hypothermic PL spectra. Besides, the dissociation energy of the trion delivers a positive correlation with the sulfur concentrations, which can be contributed to the dielectric screening phenomenon and the modulated Fermi level with the variation of sulfur in Mo(S_xSe_{1-x})₂ alloys. It is believed that the tunable bandgap and controllable values of ΔE relying on the sulfur concentrations in Mo(S_xSe_{1-x})₂ monolayer give a paradigm for the in-depth investigation of physical properties and underlying applications of 2D alloys in electronic and optoelectronic devices.

2. Experimental details

2.1. Material preparation

In this study, we fabricated the monolayer Mo(S_xSe_{1-x})₂ alloys with tunable composition on Si/SiO₂ by one-step CVD. The detailed growth procedures are illustrated in figure 1(a). For the growth of monolayer Mo(S_xSe_{1-x})₂ alloys, sulfur and selenium fine powders serving as the S source and Se source, respectively, are mixed together and placed into the first zone of furnace at upstream. The molybdenum oxide (MoO₃) powder as the Mo source mixed with sodium chloride (NaCl) particles are placed into the second zone of the quartz tube. The substrate is inverted over the MoO₃ power. Typical carrier gas is Ar/H₂ with the flow rate of 80 sccm. The growth temperature is 650°C for 3 min.

2.2. Material characterizations

The Mo(S_xSe_{1-x})₂ alloy characterizations are systematically carried out by atomic force microscopy (AFM), Raman scattering spectroscopy, and x-ray photoelectron spectroscopy (XPS). In details, AFM (Digital Instruments Icon, Bruker) with ScanAsyst modes is employed to investigate the surface morphologies and thickness of the Mo(S_xSe_{1-x})₂ alloys. The temperature-dependent PL and Raman experiments are conducted by a Jobin-Yvon LabRAM HR Evolution spectrometer and a THMSE 600 heating/cooling stage (Linkam Scientific Instruments) in the temperature ranging from 80 to 320 K with a resolution of 0.1 K. For temperature-dependent PL and Raman experiments, a 532 nm line of a diode-pumped solid state laser with the output power of 5 mW is used for the excitation. The laser beam is focused on the sample under normal incidence by applying a 50× microscope with a working distance of 18 mm to avoid the possible heating effect of the laser on the monolayer sample. An air-cooled CCD (−70 °C) with a 1024 × 256 pixels front illuminated chip is used to collect the scattered signal dispersed on 1800 grooves mm^{−1} grating for Raman measurements and 300 grooves mm^{−1} grating for PL measurements, respectively.

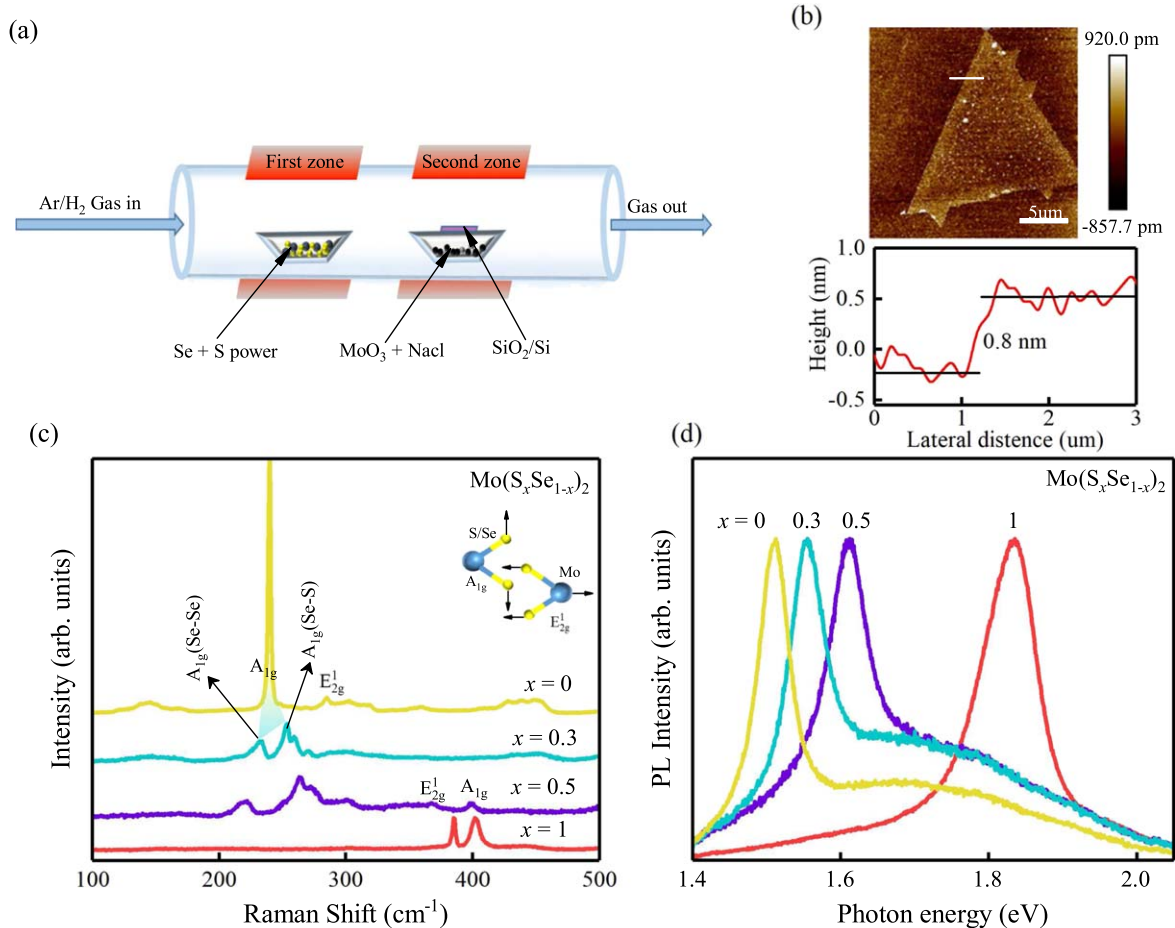


Figure 1. (a) Schematic illustration of the CVD growth for $\text{Mo}(\text{S}_x\text{Se}_{1-x})_2$. (b) AFM image and height spectrum of the monolayer $\text{Mo}(\text{S}_{0.3}\text{Se}_{0.7})_2$ nanosheet. The height profile shows that the thickness of single layer $\text{Mo}(\text{S}_{0.3}\text{Se}_{0.7})_2$ is about 0.8 nm. (c) Raman scattering and (d) photoluminescence spectra of $\text{Mo}(\text{S}_x\text{Se}_{1-x})_2$ monolayers ($x = 0 \sim 1$), respectively.

2.3. Computational details

For a better understanding of the electronic structure, we carried out the related theoretical calculations based on the density function theory (DFT), as implemented in the Vienna *ab initio* simulation package (VASP) code. [11–13] The generalized gradient approximation of Perdew–Burke–Ernzerh for the exchange–correlation function is employed. [14, 15] The monolayer MoS_2 systems are modeled by a periodic slab geometry and a vacuum layer of more than 20 Å in the z -direction is applied to avoid spurious interactions between layers caused by the periodic boundary condition. In all computations, the kinetic energy cutoff is set to be 500 eV for the plane wave expansion. All the structures are fully relaxed in conjugant gradient method, and the convergence threshold is set as 10^{-5} eV for energy and 0.01 eV/Å for force. For K-point sampling, we used the $9 \times 9 \times 1$ Monkhorst–Pack k -grid along the periodic direction. It is noticed that we first modeled the pure MoS_2 monolayer by 2×2 supercells, which contain totally 12 atoms (4 Mo atoms and 8 S atoms) to obtain the desired ternary semiconductor $\text{Mo}(\text{S}_x\text{Se}_{1-x})_2$ structures. Then the S atoms of the optimized pure MoS_2 are replaced by Se atoms randomly with various percentages (12.5%, 25%, 37.5%, 50%, 62.5%, 75%, 87.5%

and 100%), followed by the optimization operations for the stable structures.

3. Results and discussion

3.1. Morphology and Raman studies

The AFM image for the $\text{Mo}(\text{S}_{0.3}\text{Se}_{0.7})_2$ monolayer is shown in figure 1(b). It can be observed that the $\text{Mo}(\text{S}_x\text{Se}_{1-x})_2$ monolayer almost exhibits a triangle shape with the side length sizes of 20 μm. The height of the single layer $\text{Mo}(\text{S}_x\text{Se}_{1-x})_2$ nanosheet is about 0.8 nm, which is consistent with the value reported in the previous literature.[16] It is known that Raman spectroscopy, as the nondestructive analytical technique, can provide detailed information about the composition and the molecular interactions of two-dimensional materials by frequency shift and peak broadening with high resolution. Here, figure 1(c) presents the obtained Raman spectra of the monolayer $\text{Mo}(\text{S}_x\text{Se}_{1-x})_2$ at room temperature with the varying composition ($x = 0 \sim 1$). For binary MoSe_2 , the Raman features at 240.6 cm^{-1} and 286 cm^{-1} can be assigned to the out-of-plane A_{1g} and in-plane E_{2g}^1 mode, respectively. [17–19] For MoS_2 nanosheet, the above

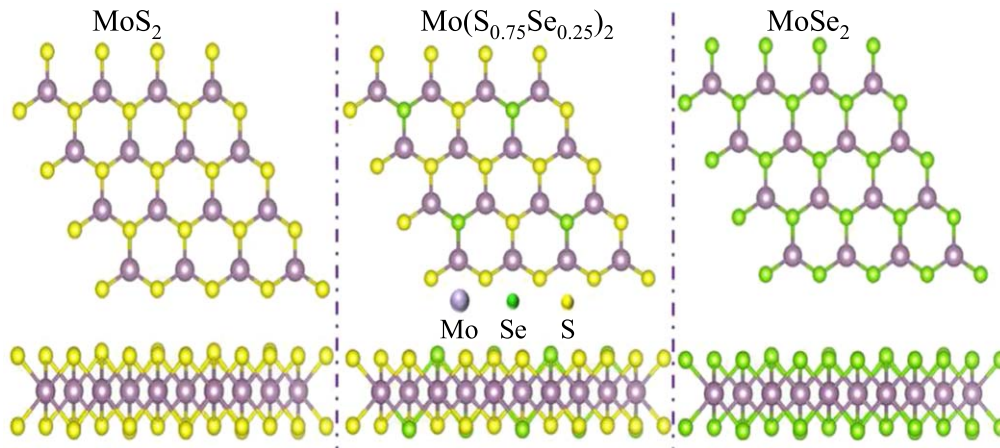


Figure 2. Top and side views of the atomic structures of MoS₂ (left), Mo(S_{0.75}Se_{0.25})₂ alloy (middle) and MoSe₂ (right) 2D TMDs. Note that the systems consist of three layers of atoms.

mentioned two peaks of the in-plane A_{1g} mode and the out-of-plane E_{2g}^1 locate at 404.7 cm^{-1} and 387.4 cm^{-1} , respectively. Evidently, both of the MoSe₂-related modes at low frequency ($200\text{--}300\text{ cm}^{-1}$) and the MoS₂-related peaks at high frequency ($350\text{--}410\text{ cm}^{-1}$) can be recorded in the Raman spectra of Mo(S_{*x*}Se_{*1-x*})₂ alloy. In details, at lower frequency, the MoSe₂-related A_{1g} mode splits into two phonon modes, which are denoted as $A_{1g}(\text{Se--Se})$ and $A_{1g}(\text{Se--S})$, respectively. This phenomenon can be explained by the induced vibrations with out-of-plane weight in the vicinity of A_{1g} via the sulfur atom in the host lattice of MoSe₂. With increasing the S content, the $A_{1g}(\text{Se--S})$ mode shows a blue-shift trend. Note that the similar mode behavior has also been reported in Mo(S_{*x*}Se_{*1-x*})₂ monolayer films. [20] On the contrary, $A_{1g}(\text{Se--Se})$ mode exhibits an obvious red-shift trend. While at higher frequency, the branches can be derived from the MoS₂-related E_{2g}^1 and A_{1g} modes. It can be seen that all of the MoS₂-related peaks tend to shift toward the lower frequency with increasing the Se content in Mo(S_{*x*}Se_{*1-x*})₂ mixed crystals, which hints at that the distortion of Mo–S bonds and the softened vibration of E_{2g}^1 and A_{1g} modes of MoS₂ induced by Se atoms. It is emphasized that the chemical states and S contents *x* in Mo(S_{*x*}Se_{*1-x*})₂ alloy have been confirmed by XPS analysis and shown in figure S1 (supporting information is available at stacks.iop.org/NANO/31/155703/mmedia). Figure 1(d) presents the corresponding PL spectra of monolayer Mo(S_{*x*}Se_{*1-x*})₂ nanosheets. As we can see, the obtained bandgap delivers a continuously tunable value from 1.52 eV (MoSe₂) to 1.85 eV (MoS₂) as the function of S content. It is believed that the Mo(S_{*x*}Se_{*1-x*})₂ alloys with the adjustable electronic bandgap enrich 2D material family, which leads to a wider uses of the alloy materials in the potential optoelectronic applications.

3.2. Theoretical analysis

In order to further understand the electronic structure of the monolayer Mo(S_{*x*}Se_{*1-x*})₂ alloys with different S content, the electronic band structure has been calculated by the first principle calculations. Unlike the Janus structure that the S

and Se atoms are located regularly in opposite positions in the lattice, [21] the positions of these two atoms in the Mo(S_{*x*}Se_{*1-x*})₂ alloy synthesized by conventional doping are randomly distributed in the present work. A cartoon illustrating the atomic structure of a mixed 2D TMD, along with the constituent parent materials is shown in figure 2. In practice, the Mo(S_{*x*}Se_{*1-x*})₂ alloys are built from the MoS₂ monolayer with some of the S atoms are randomly replaced by the Se atoms. As shown in figures 3(a)–(e), all the structures show a direct band gap with the valence-band maximum (VBM) and conduction-band minimum (CBM) located at the K point in the Brillouin zone. The S content dependent calculated bandgap values are plotted in figure 3(f). Note that the direct bandgap of the Mo(S_{*x*}Se_{*1-x*})₂ alloy nanosheets, located at the visible spectral range, shows a continuous increase as the rising up of S content, which agree well with the experimental results by PL spectrum. The values of the band gap are almost the same for the different positions of substituting atoms of Se in the Mo(S_{*x*}Se_{*1-x*})₂ alloy. The detailed description are shown in figure S2 (supporting information). The work function (Φ) of the monolayer Mo(S_{*x*}Se_{*1-x*})₂ nanosheets, used as an intrinsic reference for the band alignment, [22] can be calculated using the following equation:

$$\Phi = E_{\text{vac}} - E_{\text{F}}, \quad (1)$$

where E_{vac} is the energy level of a stationary electron in the vacuum nearby the surface. E_{F} is the Fermi energy level of the corresponding systems. Figures 3(g)–(k) demonstrate the electrostatic potentials of monolayer Mo(S_{*x*}Se_{*1-x*})₂ alloy. The work functions of the MoS₂, Mo(S_{0.25}Se_{0.75})₂, Mo(S_{0.5}Se_{0.5})₂, Mo(S_{0.75}Se_{0.25})₂ and MoSe₂ are calculated to be 5.10, 5.21, 5.35, 5.50 and 5.69 eV, respectively, which deliver an evident enlargement continuously along with increasing the S content (figure 3(l)). Thus, the larger work function of the MoS₂ than that of the MoSe₂ would lead to a higher fermi level of MoS₂ than that of MoSe₂. It is worth mentioning that this result is related to the variation of the dissociation energy of the trion in Mo(S_{*x*}Se_{*1-x*})₂ alloys with different S content, which would be systematically discussed below.

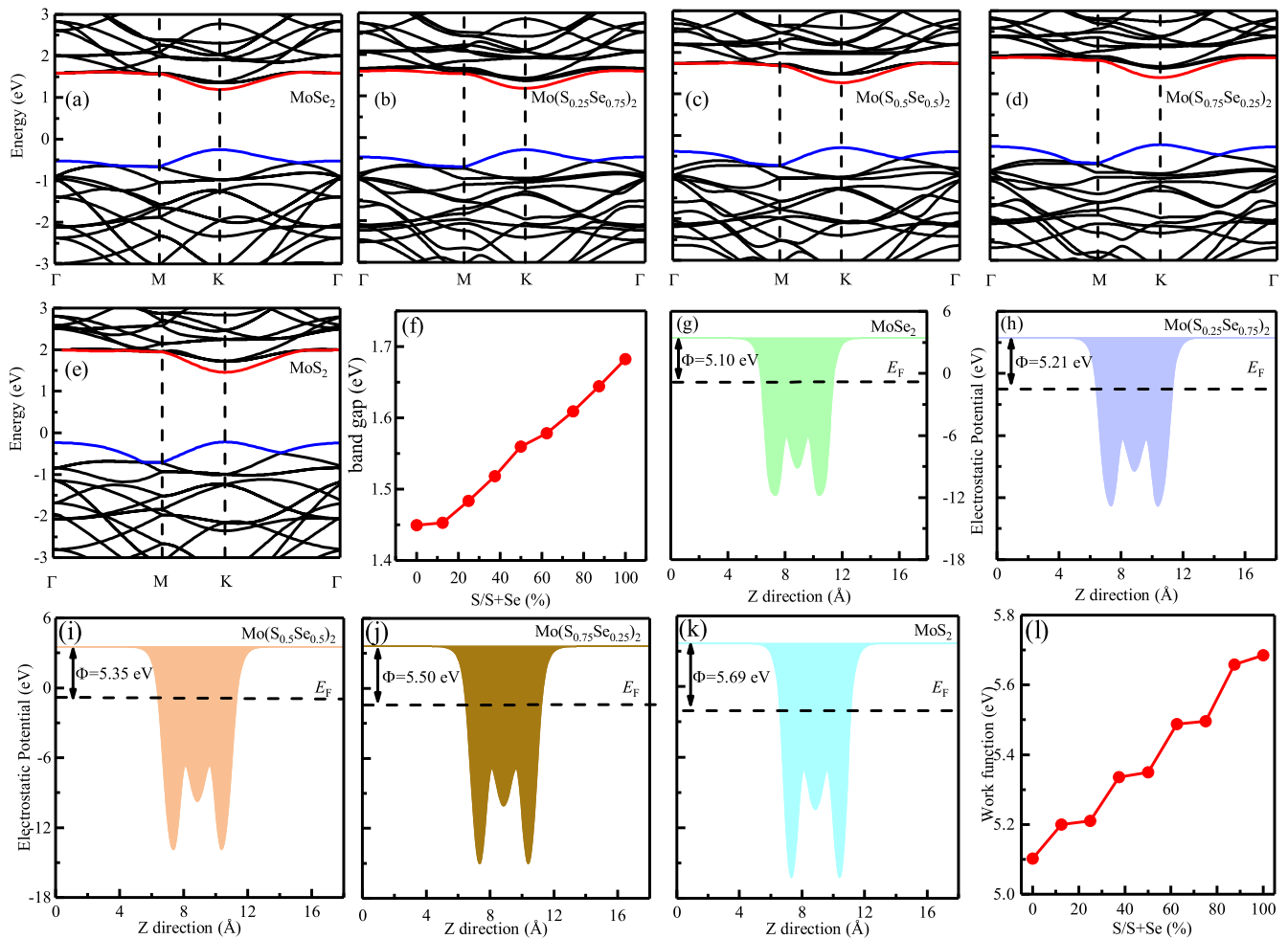


Figure 3. The electronic band structures for $\text{Mo}(\text{S}_x\text{Se}_{1-x})_2$ alloy nanosheets: (a) MoSe_2 , (b) $\text{Mo}(\text{S}_{0.25}\text{Se}_{0.75})_2$, (c) $\text{Mo}(\text{S}_{0.5}\text{Se}_{0.5})_2$, (d) $\text{Mo}(\text{S}_{0.75}\text{Se}_{0.25})_2$, (e) MoS_2 , respectively. (f) Variation of the band gap with respect to the sulfur mole ratio for $\text{Mo}(\text{S}_x\text{Se}_{1-x})_2$ alloy nanosheets. The electrostatic potential of (g) MoSe_2 , (h) $\text{Mo}(\text{S}_{0.25}\text{Se}_{0.75})_2$, (i) $\text{Mo}(\text{S}_{0.5}\text{Se}_{0.5})_2$, (j) $\text{Mo}(\text{S}_{0.75}\text{Se}_{0.25})_2$, (k) MoS_2 , respectively. (l) The work function variation of $\text{Mo}(\text{S}_x\text{Se}_{1-x})_2$ alloy with the relative concentration of sulfur atoms.

3.3. Temperature dependent optical characterization

Figures 4(a)–(b) show the temperature dependence of frequency shift with the step of 40 K for monolayer $\text{Mo}(\text{S}_{0.3}\text{Se}_{0.7})_2$ and $\text{Mo}(\text{S}_{0.5}\text{Se}_{0.5})_2$, respectively. The phonon frequency can be derived by fitting the Lorentzian functions for each Raman mode as a function of temperature given by the following formula: [23] $\omega(T) = \omega_0 + \chi T$. Where ω_0 is the phonon frequency of $A_{1g}(\text{Se}-\text{Se})$, $A_{1g}(\text{Se}-\text{S})$, MoS_2 -related A_{1g} and E_{2g}^1 vibration modes at zero Kelvin temperature, χ is the first order temperature coefficient of each vibration mode. Figures 4(c)–(h) show the Raman active phonon as a function of temperature for the $\text{Mo}(\text{S}_{0.3}\text{Se}_{0.7})_2$ and $\text{Mo}(\text{S}_{0.5}\text{Se}_{0.5})_2$ nanosheets. The linearly downward shift can be observed in each Raman active phonon mode with increasing the temperature from 80 to 320 K. The temperature coefficient and the difference of phonon frequency ($\Delta\omega$) for $\text{Mo}(\text{S}_x\text{Se}_{1-x})_2$ ($x = 0, 0.3, 0.5$ and 1) nanosheets are shown in table 1. For a better comparison, the temperature dependent Raman spectra and phonon frequency of the pure MoS_2 and MoSe_2 samples are provided in figure S3 (supporting information). It reveals the similar temperature-dependent behavior for that of MoS_2 and MoSe_2 .

In monolayer $\text{Mo}(\text{S}_x\text{Se}_{1-x})_2$ alloys, the values of $\Delta\omega$ with the temperature variation from 80 K to 320 K for $A_{1g}(\text{Se}-\text{Se})$ and $A_{1g}(\text{Se}-\text{S})$ modes are fitted to be 2.63 and 2.82 cm^{-1} for $x = 0.3$, while 2.01 and 2.34 cm^{-1} for $x = 0.5$, respectively. It can be found that both the $A_{1g}(\text{Se}-\text{S})$ mode and $A_{1g}(\text{Se}-\text{Se})$ mode in $\text{Mo}(\text{S}_{0.3}\text{Se}_{0.7})_2$ alloy show a larger frequency shift with the temperature, which hints that the MoSe_2 -related A_{1g} mode is more sensitive to the Se content. For the MoS_2 -related modes, $\Delta\omega$ in the A_{1g} and E_{2g}^1 phonon modes are assigned to be 4.24 cm^{-1} and 2.81 cm^{-1} for MoS_2 , 2.23 cm^{-1} and 3.02 cm^{-1} for $\text{Mo}(\text{S}_{0.5}\text{Se}_{0.5})_2$ alloy, respectively. Note that $\Delta\omega$ for E_{2g}^1 mode is larger than that of the A_{1g} mode in the monolayer $\text{Mo}(\text{S}_{0.5}\text{Se}_{0.5})_2$ nanosheet, which is in contrast to the behavior in monolayer MoS_2 . It can be explained by the following two aspects. On the one hand, both A_{1g} mode and E_{2g}^1 mode are softened with the temperature, which is attributed to anharmonic contributions to the interatomic potential energy mediated by phonon–phonon interactions. [24] On the other hand, the A_{1g} mode and E_{2g}^1 mode show distinct electron concentration dependence; the A_{1g} mode is softened with the electron concentration, whereas

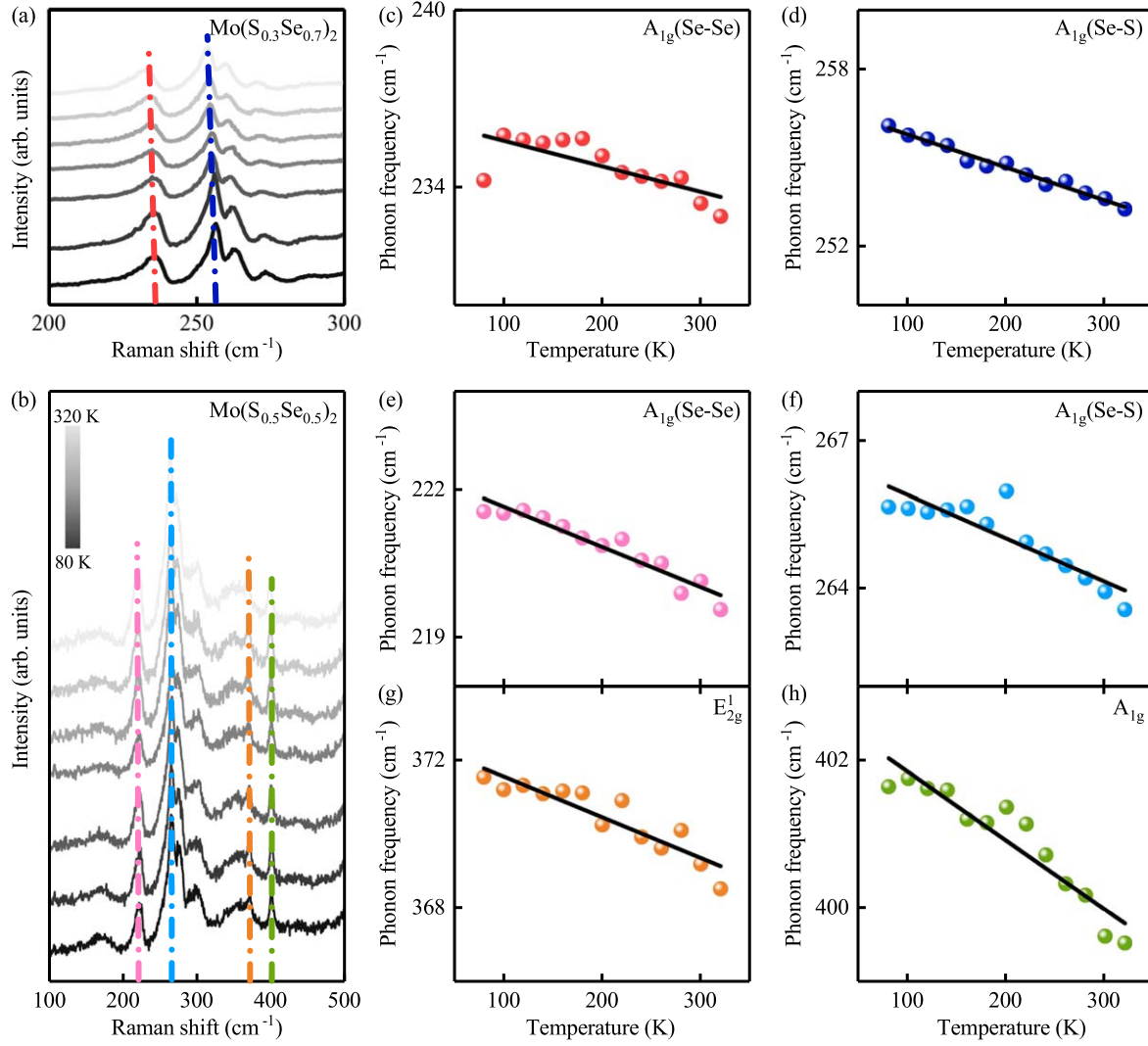


Figure 4. Temperature dependent Raman spectra of monolayer $\text{Mo}(\text{S}_x\text{Se}_{1-x})_2$ nanosheets: (a) $\text{Mo}(\text{S}_{0.3}\text{Se}_{0.7})_2$ and (b) $\text{Mo}(\text{S}_{0.5}\text{Se}_{0.5})_2$, respectively. Phonon frequency of the main vibrational modes as a function of temperature for single layer $\text{Mo}(\text{S}_x\text{Se}_{1-x})_2$ nanosheets: (c)–(d) $\text{Mo}(\text{S}_{0.3}\text{Se}_{0.7})_2$, (e)–(f) $\text{Mo}(\text{S}_{0.5}\text{Se}_{0.5})_2$, respectively.

Table 1. The temperature evolution of the main vibrational modes for the $\text{Mo}(\text{S}_x\text{Se}_{1-x})_2$ nanosheets with the sulfur content from 0 to 1.

Monolayer TMDCs	Phonon mode	Temperature coefficient χ ($\text{cm}^{-1} \text{K}^{-1}$)	$\Delta\omega$ (cm^{-1})
MoSe_2	A_{1g}	−0.0099	2.26
MoSe_2	E_{2g}	−0.0085	2.28
$\text{Mo}(\text{S}_{0.3}\text{Se}_{0.7})_2$	$A_{1g}(\text{Se-Se})$	−0.0087	2.63
$\text{Mo}(\text{S}_{0.3}\text{Se}_{0.7})_2$	$A_{1g}(\text{Se-S})$	−0.0111	2.82
$\text{Mo}(\text{S}_{0.5}\text{Se}_{0.5})_2$	$A_{1g}(\text{Se-Se})$	−0.0082	2.01
$\text{Mo}(\text{S}_{0.5}\text{Se}_{0.5})_2$	$A_{1g}(\text{Se-S})$	−0.0088	2.34
$\text{Mo}(\text{S}_{0.5}\text{Se}_{0.5})_2$	A_{1g}	−0.0093	2.23
$\text{Mo}(\text{S}_{0.5}\text{Se}_{0.5})_2$	E_{2g}	−0.0110	3.02
MoS_2	A_{1g}	−0.0185	4.24
MoS_2	E_{2g}	−0.0115	2.81

the E_{2g}^1 mode remains essentially inert. [25] The 2D carrier concentration in sulfides is about two orders of magnitude higher than that in selenides. [26] Thus, the increased selenide content in the $\text{Mo}(\text{S}_x\text{Se}_{1-x})_2$ alloys could result in the increasing of carrier concentration in the MoS_2 , as compared with that in the $\text{Mo}(\text{S}_{0.5}\text{Se}_{0.5})_2$ alloy.

Figures 5(a)–(c) show the PL spectra for monolayer MoSe_2 and $\text{Mo}(\text{S}_x\text{Se}_{1-x})_2$ nanosheets at $T = 80$ K. In order to further explore the evolution of PL spectra, the Gaussian function is employed to fit the obtained spectra. Interestingly, the characteristics of all PL spectra can be classified to two distinct transitions, which are defined as neutral exciton (X, a higher-energy one) and charged exciton or trion (T, a lower energy one) emissions, respectively. [27–30] The formation of two split peaks for X and T is because of the strong

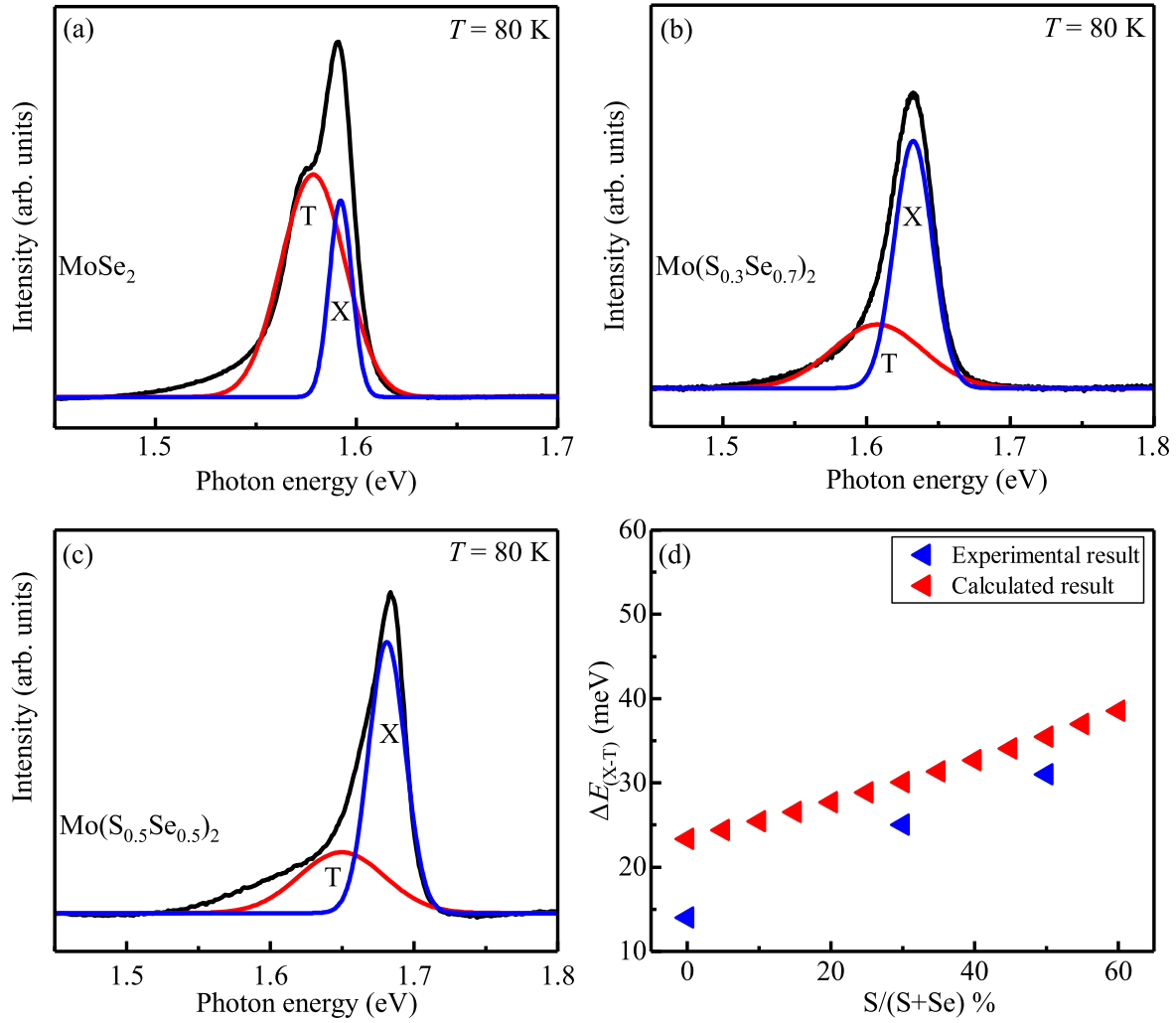


Figure 5. Typical PL spectra measured at $T = 80$ K and the multiple-peak fitting by using the Gaussian function for monolayer $\text{Mo}(\text{S}_x\text{Se}_{1-x})_2$ nanosheets: (a) MoSe_2 , (b) $\text{Mo}(\text{S}_{0.3}\text{Se}_{0.7})_2$, (c) $\text{Mo}(\text{S}_{0.5}\text{Se}_{0.5})_2$, respectively. (d) The ΔE versus the sulfur ratio in monolayer $\text{Mo}(\text{S}_x\text{Se}_{1-x})_2$ analyzed by the experiment and theoretical calculation.

spin-orbit coupling and the lack of inversion symmetry, which lead to valley-contrasting strong spin splitting of valence and conducting bands. [31–33] Note that similar exciton-emission features have also been observed in WS_2 and other binary 2D TMDCs. [34–37] Besides, for binary MoSe_2 and ternary $\text{Mo}(\text{S}_x\text{Se}_{1-x})_2$ alloys, the PL intensity and peak position in exciton and trion present totally different behavior. In MoSe_2 , the trion dominates the PL spectrum. In contrast, the PL intensity of exciton is stronger than that of trion for $\text{Mo}(\text{S}_{0.3}\text{Se}_{0.7})_2$ and $\text{Mo}(\text{S}_{0.5}\text{Se}_{0.5})_2$ alloys, which can be contributed to the two-dimensional carrier gas concentration.

The difference (ΔE) between the emission energy of the exciton (E_X) and trion (E_T) for the MoSe_2 and $\text{Mo}(\text{S}_x\text{Se}_{1-x})_2$ ($x = 0.3, 0.5$) nanosheets, it can be given by the formula: [38]

$$\Delta E = E_X - E_T = E_{b,T} + E_F, \quad (2)$$

where the parameter $E_{b,T}$ is the trion binding energy. The binding energy is defined as the dissociation energy in the limit of infinitively small doping ($E_F = 0$), which is the energy needed to promote one electron from the trion to the

bottom of the conduction. In order to further elucidate the sulfur-content dependence of the ΔE value in monolayer $\text{Mo}(\text{S}_x\text{Se}_{1-x})_2$, the computational results based on the ‘effective exciton’ model are additionally demonstrated to validate the experimental findings.

The Schrodinger equation for the wave-function of the electron-hole relative motion in the plane of the layer $\Psi(\rho)$ in cylindrical coordinates reads

$$\left[\frac{-\hbar^2}{2\mu} \left(\frac{\partial^2}{\partial \rho^2} + \frac{1}{\rho} \frac{\partial}{\partial \rho} \right) - \int_0^\infty J_0(k\rho) V_C k dk - E_{ex} \right] \Psi(\rho) = 0, \quad (3)$$

where $J_0(k\rho)$ is the zeroth order Bessel function, $\mu = \frac{m_e m_h}{m_e + m_h}$ is the reduced mass of electron-hole relative motion, and V_C is the screened Coulomb potential, which is can be written as [39]

$$V_C = \frac{e^2 \arctan(\tilde{k}/k)}{\epsilon k (1 + (\kappa/k)(1 - \Theta(k - 2k_F) \sqrt{1 - (2k_F/k)^2})} \quad (4)$$

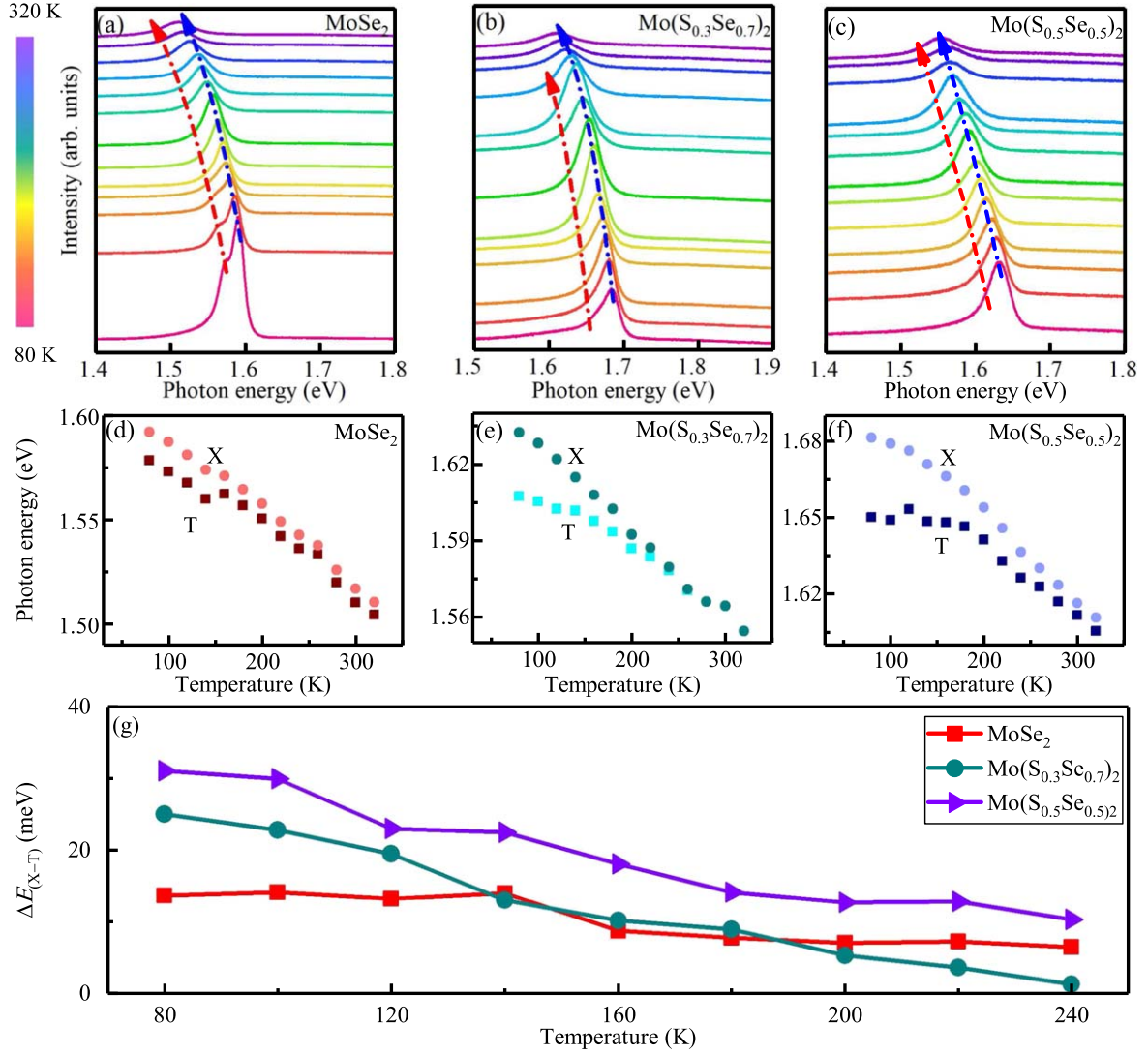


Figure 6. (a)–(c) Photoluminescence spectra as a function of temperature for monolayer $\text{Mo}(\text{S}_x\text{Se}_{1-x})_2$ nanosheets: MoSe_2 , $\text{Mo}(\text{S}_{0.3}\text{Se}_{0.7})_2$, and $\text{Mo}(\text{S}_{0.5}\text{Se}_{0.5})_2$, respectively. The E_X and E_T as a function of temperature for single layer $\text{Mo}(\text{S}_x\text{Se}_{1-x})_2$: (d) MoSe_2 , (e) $\text{Mo}(\text{S}_{0.3}\text{Se}_{0.7})_2$, (f) $\text{Mo}(\text{S}_{0.5}\text{Se}_{0.5})_2$, respectively. (g) The temperature dependence of the ΔE in monolayer $\text{Mo}(\text{S}_x\text{Se}_{1-x})_2$ nanosheets.

here, ϵ is the dielectric constant, g_v is the valley degeneracy factor, $\kappa = \frac{2g_v m_e e^2}{\epsilon \hbar^2}$ is the screening constant, and $\tilde{k} = 2\pi/0.75L$, L is the thickness of a layer.

The trial function of the exciton ($\Psi(\rho)$) in equation (3), it can be given by the formula: [40]

$$\Psi(\rho) = \int_0^\infty J_0(k\rho) f(k) k dk, \quad (5)$$

$$f(k) = \frac{B}{(A + k^2)^{3/2}} \Theta(k - k_F), \quad (6)$$

where $\Theta(k - k_F)$ is the Heaviside function, $k_F = \sqrt{2\pi n_{2D}}$, n_{2D} is the density of free carriers, A is a variational parameter, inversely proportional to the squared exciton Bohr radius, and $B^2 = \frac{2}{\pi} A^2$. Varying the parameter A , the exciton binding energy can be found as the minimum value of E_{ex} [9], where

$$E_{\text{ex}} = \int_0^\infty \Psi(\rho) \left[\frac{-\hbar^2}{2\mu} \frac{1}{\rho} \frac{\partial}{\partial \rho} \left(\rho \frac{\partial}{\partial \rho} \right) - \int_0^\infty J_0(k\rho) V_C k dk \right] \times \Psi(\rho) 2\pi \rho d\rho. \quad (7)$$

For the trion case, the two electrons are assumed in the singlet state, which can be characterized by orthogonal spin functions and identical spatial wave functions. The trion wave function can be expressed as

$$\Psi(\rho) = \int_0^\infty J_0(k\rho) f_{\text{tr}}(k) k dk, \quad (8)$$

$$f_{\text{tr}}(k) = \frac{B}{(A + k^2)^{3/2}} \Theta(k - k_F) + \frac{C}{(D + k^2)^{3/2}} \Theta(k_F - k). \quad (9)$$

The trion binding energy can be good estimated by the equation (7) under the minimization over both variational parameter A and D .

The variation in figure 5(d) indicates that the ΔE show an upward shift trend along with increasing the S content in $\text{Mo}(\text{S}_x\text{Se}_{1-x})_2$ alloys from the experiment and theoretical calculation. It shows that the experiment result matches well with the theoretical result. Based on the equation (2), the variation of the ΔE value can be ascribed to the varied $E_{b,T}$ and E_F along with the S content. Note that the effective exciton mass decreases with lighter chalcogen species, subsequently the decreased dielectric screening effect results in the systematic increase in the $E_{b,T}$. [41] Thus, a blue-shift trend of the $E_{b,T}$ can be observed with the sulfur content. In addition, the E_F of the MoS_2 is larger than that of the MoSe_2 according to the theoretical calculation, as shown in figure 2. Therefore, the dissociation energy of trion gradually enlarges with increasing the S content. Furthermore, it also could be related to the strong difference in two-dimensional carrier concentration, which is higher in MoS_2 than that in MoSe_2 due to the additional electron excited over the Fermi energy during the radiative recombination of an electron-hole pair in a trion complex. [26]

Figures 6(a)–(c) present the evolution of PL spectra as a function of temperature for monolayer MoSe_2 and $\text{Mo}(\text{S}_x\text{Se}_{1-x})_2$. The corresponding PL spectra for monolayer MoS_2 are provided in figure S4 (supporting information) for comparison. As we can see, all of the PL features show an evident red-shift and apparent attenuation with increasing the temperature, which can be attributed to the increasing nonradiative electron-hole recombination rate. [42–44] With the temperature above 120 K, the PL intensity of the trion for the binary MoSe_2 decreased as the rising up of temperature. With the temperature increasing above 240 K, however, the trion peak for the alloy $\text{Mo}(\text{S}_{0.3}\text{Se}_{0.7})_2$ gradually quenches and the PL spectra are dominated by the exciton behavior. For a clear observation, figures 6(d)–(f) demonstrate the E_X and E_T as a function of the temperature for monolayer $\text{Mo}(\text{S}_x\text{Se}_{1-x})_2$ ($x = 0, 0.3$ and 0.5) nanosheets, respectively. It clearly shows that the E_X exhibits a monotonous decrease with the increasing of temperature for all the three samples. However, the evolution of E_T in the $\text{Mo}(\text{S}_{0.5}\text{Se}_{0.5})_2$ alloy delivers a mountain-shaped transition as a function of temperature, which could be attributed to the effect of the sulfur content. Therefore, it could propose that the variation of E_X and E_T with the increasing of temperature result from the electron–phonon interactions and slight changes in bond lengths, which can be described using the semi-empirical formula of O’ Donnell: [45]

$$E_g(T) = E_g(0) - S < \hbar\omega > \left[\coth\left(\frac{< \hbar\omega >}{2k_B T}\right) - 1 \right], \quad (10)$$

where $E_g(0)$ is the emission energy at 0 K, S is the Huang–Rhys factor that represents the coupling strength of the exciton and phonon, and $< \hbar\omega >$ is the average phonon energy, k_B is the Boltzmann constant, T is the absolute temperature in Kelvin. Figure 6(g) shows the temperature dependence of the ΔE for the sample of $\text{Mo}(\text{S}_x\text{Se}_{1-x})_2$ ($x = 0.3, 0.5$ and 1). It can be seen that the ΔE is gradually reduced as the increasing of temperature. It can be explained that the carriers are frozen out onto the donor levels as the temperature increasing, thus leading to the reduced carriers content in the donor level and the decreased ΔE values at higher temperature. Therefore, we could conclude that the present

study lay the foundation for further explore the potential application of the 2D alloys in electronic and optoelectronic devices, in terms of the controllable values of the ΔE depending on the sulfur concentrations and temperature in monolayer $\text{Mo}(\text{S}_x\text{Se}_{1-x})_2$.

4. Conclusions

In conclusion, we conducted the systematical study of the intrinsic physical phenomena of monolayer $\text{Mo}(\text{S}_x\text{Se}_{1-x})_2$ alloys by both optical methods and theoretical analysis. With various compositions of sulfur, the calculated band gap values of monolayer $\text{Mo}(\text{S}_x\text{Se}_{1-x})_2$ alloy increases with the sulfur content, which can be confirmed by the PL spectra at room temperature. The temperature-dependent Raman spectra demonstrate the different trends of $\Delta\omega$ for A_{1g} and E_{2g}^1 in binary MoS_2 and $\text{Mo}(\text{S}_{0.5}\text{Se}_{0.5})_2$ alloy, which is attributed to the anharmonicity and electron concentration. Furthermore, the evolution of PL spectra as a function of temperature indicates that the dissociation energy of the trion can be remarkably tuned by the sulfur mole content. Combining with the theoretical calculation, we could conclude that the experimental results can be contributed to the difference of the dielectric screening effect and the Fermi energy between the monolayer MoSe_2 and $\text{Mo}(\text{S}_x\text{Se}_{1-x})_2$. In consequence, it is believed that the tunable optical transition energies and effectively controllable band gap engineering of monolayer $\text{Mo}(\text{S}_x\text{Se}_{1-x})_2$ alloys can create more opportunities for 2D alloys to use in the fields of electronics and optoelectronics.

Acknowledgments

This work was financially supported by the National Key R&D Program of China (grant nos. 2017YFA0303403 and 2018YFB0406500), the National Natural Science Foundation of China (grant nos. 91833303, 61974043, and 61674057), Projects of Science and Technology Commission of Shanghai Municipality (grant nos. 18JC1412400, 18YF1407200, 18YF1407000, and 19511120100), and the Program for Professor of Special Appointment (Eastern Scholar) at Shanghai Institutions of Higher Learning.

ORCID iDs

Zhigao Hu  <https://orcid.org/0000-0003-0575-2191>

References

- [1] Li M J *et al* 2018 High mobilities in layered InSe transistors with indium-encapsulation-induced surface charge doping *Adv. Mater.* **30** 1803690
- [2] Yin Z Y, Li H, Li H, Jiang L, Sun Y M, Lu G, Zhang Q, Chen X D and Zhang H 2011 Single-layer MoS_2 phototransistors *ACS Nano* **6** 74–80

- [3] Sundaram R S, Engel M, Lombardo A, Krupke R, Ferrari A C, Avouris P and Steiner M 2013 Electroluminescence in single layer MoS₂ *Nano Lett.* **13** 1416–21
- [4] Zeng H L, Dai J F, Yao W, Xiao D and Cui X D 2012 Valley polarization in MoS₂ monolayers by optical pumping *Nat. Nanotechnol.* **7** 490
- [5] Gong Y J et al 2013 Band gap engineering and layer-by-layer mapping of selenium-doped molybdenum disulfide *Nano Lett.* **14** 442–9
- [6] Duan X D et al 2015 Synthesis of WS₂xSe_{2–2x} alloy nanosheets with composition-tunable electronic properties *Nano Lett.* **16** 264–9
- [7] Cao L Y 2015 Two-dimensional transition-metal dichalcogenide materials: toward an age of atomic-scale photonics *MRS Bull.* **40** 592–9
- [8] Mak K F and Shan J 2016 Photonics and optoelectronics of 2D semiconductor transition metal dichalcogenides *Nat. Photon.* **10** 216
- [9] Lundt N, Cherotchenko E, Iff O, Fan X, Shen Y, Bigenwald P, Kavokin A V, Höfling S and Schneider C 2018 The interplay between excitons and trions in a monolayer of MoSe₂ *Appl. Phys. Lett.* **112** 031107
- [10] Sun H M, Wang J Y, Wang F, Xu L P, Jiang K, Shang L Y, Hu Z G and Chu J H 2018 Enhanced exciton emission behavior and tunable band gap of ternary W(S_xSe_{1–x})₂ monolayer: temperature dependent optical evidence and first-principles calculations *Nanoscale* **10** 11553–63
- [11] Blöchl P E 1994 Projector augmented-wave method *Phys. Rev. B* **50** 17953–79
- [12] Kresse G and Hafner J 1993 Ab initio molecular dynamics for liquid metals *Phys. Rev. B* **47** 558
- [13] Kresse G and Hafner J 1994 Ab initio molecular-dynamics simulation of the liquid-metal-amorphous-semiconductor transition in germanium *Phys. Rev. B* **49** 14251
- [14] Perdew J P, Bruke K and Ernzerhof M 1996 Generalized gradient approximation made simple *Phys. Rev. Lett.* **77** 3865
- [15] Kerber T, Sierka M and Sauer J 2008 Application of semiempirical long-range dispersion corrections to periodic systems in density functional theory *J. Comput. Chem.* **29** 2088–97
- [16] Zhang W T, Li X D, Jiang T T, Song J L Q, Lin Y, Zhu L X and Xu X L 2015 CVD synthesis of Mo_{1–x}W_xS₂ and MoS_{2(1–x)}Se_{2x} alloy monolayers aimed at tuning the bandgap of molybdenum disulfide *Nanoscale* **7** 13554
- [17] Tonndorf P et al 2013 Photoluminescence emission and Raman response of monolayer MoS₂, MoSe₂, and WSe₂ *Opt. Express* **21** 4908–16
- [18] Chen S Y, Zheng C X, Fuhrer M S and Yan J 2015 Helicity-resolved Raman scattering of MoS₂, MoSe₂, WS₂, and WSe₂ atomic layers *Nano Lett.* **15** 2526–32
- [19] Sahin H, Tongay S, Horzum S, Fan W, Zhou J, Li J, Wu J and Peeters F M 2013 Anomalous Raman spectra and thickness-dependent electronic properties of WSe₂ *Phys. Rev. B* **87** 165409
- [20] Mann J et al 2014 2-Dimensional transition metal dichalcogenides with tunable direct band gaps: MoS_{2(1–x)}Se_{2x} monolayers *Adv. Mater.* **26** 1399–404
- [21] Lu A-Y et al 2017 Janus monolayers of transition metal dichalcogenides *Nat. Nanotechnol.* **12** 744–50
- [22] Liu J J and Hua E 2015 Electronic structure and absolute band edge position of tetragonal AgInS₂ photocatalyst: a hybrid density functional study *Mater. Sci. Semicond. Process.* **40** 446–52
- [23] Zouboulis E S and Grimsditch M 1991 Raman scattering in diamond up to 1900 K *Phys. Rev. B* **43** 12490–3
- [24] Tongay S, Zhou J, Ataca C, Lo K, Matthews T S, Li J B, Grossman J C and Wu J Q 2012 Thermally driven crossover from indirect toward direct bandgap in 2D semiconductors: MoSe₂ versus MoS₂ *Nano Lett.* **12** 5576–80
- [25] Lanzillo N A et al 2013 Temperature-dependent phonon shifts in monolayer MoS₂ *Appl. Phys. Lett.* **103** 093102
- [26] Jadcak J, Kutrowska-Girzycka J, Kapuściński P, Huang Y S, Wójs A and Bryja L 2017 Probing of free and localized excitons and trions in atomically thin WSe₂, WS₂, MoSe₂ and MoS₂ in photoluminescence and reflectivity experiments *Nanotechnology* **28** 395702
- [27] Ross J S et al 2013 Electrical control of neutral and charged excitons in a monolayer semiconductor *Nat. Commun.* **4** 1474
- [28] Mitioglu A A, Plochocka P, Jadcak J N, Escoffler W, Rikken G L J A, Kulyuk L and Maude D K 2013 Optical manipulation of the exciton charge state in single-layer tungsten disulfide *Phys. Rev. B* **88** 245403
- [29] Singh A et al 2016 Trion formation dynamics in monolayer transition metal dichalcogenides *Phys. Rev. B* **93** 041401
- [30] Godde T et al 2016 Exciton and trion dynamics in atomically thin MoSe₂ and WSe₂: effect of localization *Phys. Rev. B* **94** 165301
- [31] Kadantsev E S and Hawrylak P 2012 Electronic structure of a single MoS₂ monolayer *Solid State Commun.* **152** 909–13
- [32] Liu G B, Shan W Y, Yao Y G, Yao W and Xiao D 2013 Three-band tight-binding model for monolayers of group-VIB transition metal dichalcogenides *Phys. Rev. B* **88** 085433
- [33] Dery H and Song Y 2015 Polarization analysis of excitons in monolayer and bilayer transition-metal dichalcogenides *Phys. Rev. B* **92** 125431
- [34] Ye Y X, Dou X M, Ding K, Jiang D S, Yang F H and Sun B Q 2016 Pressure-induced K-Λ crossing in monolayer WSe₂ *Nanoscale* **8** 10843–8
- [35] Jones A M et al 2013 Optical generation of excitonic valley coherence in monolayer WSe₂ *Nat. Nanotech.* **8** 634
- [36] Wang Y L, Cong C X, Yang W H, Shang J Z, Peimyoo N, Chen Y and Kang J Y 2015 Strain-induced direct-indirect bandgap transition and phonon modulation in monolayer WS₂ *Nano Res.* **8** 2562–72
- [37] Mak K F, He K L, Lee C, Lee G H, Hone J, Heinz T F and Shan J 2013 Tightly bound trions in monolayer MoS₂ *Nat. Mater.* **12** 207
- [38] Huard V, Cox R T, Saminadayar K, Arnoult A and Tatarenko S 2000 Bound states in optical absorption of semiconductor quantum wells containing a two-dimensional electron gas *Phys. Rev. Lett.* **84** 187
- [39] Klochikhin A A, Kochereshko V P, Besombes L, Karczewski G, Wojtowicz T and Kossut J 2011 Plasmon mechanism of the trion emission band broadening in quantum wells *Phys. Rev. B* **83** 235329
- [40] Pikus F G 1992 Excitons in quantum wells with a two-dimensional electron gas *Sov. Phys. Semicond.* **26** 26–33
- [41] Ramasubramanian A 2012 Large excitonic effects in monolayers of molybdenum and tungsten dichalcogenides *Phys. Rev. B* **86** 115409
- [42] Ji C Y et al 2015 Temperature-dependent photoluminescence of Ag₂Se quantum dots *J. Phys. Chem. C* **119** 13841–6
- [43] Makino T, Tamura K, Chia C H, Segawa Y, Kawasaki M, Ohtomo A and Koinuma H 2003 Temperature quenching of exciton luminescence intensity in ZnO/(Mg, Zn)O multiple quantum wells *J. Appl. Phys.* **93** 5929–33
- [44] Fonoberov V A, Alim K A, Balandin A A, Xu F X and Liu J L 2006 Photoluminescence investigation of the carrier recombination processes in ZnO quantum dots and nanocrystals *Phys. Rev. B* **73** 165317
- [45] O'Donnell K P and Chen X 1991 Temperature dependence of semiconductor band gaps *Appl. Phys. Lett.* **58** 2924–6